Journal of Materials Chemistry A

Accepted Manuscript

ROYAL SOCIETY OF CHEMISTRY

www.rsc.org/materialsA

Single-crystalline $Ni(OH)_2$ nanosheets vertically aligned on three-dimensional nanoporous metal for high-performance asymmetric supercapacitors

Chao Hou, Xing-You Lang,* Zi Wen, Yong-Fu Zhu, Ming Zhao, Jian-Chen Li, Wei-Tao Zheng, Jian-She Lian, Qing Jiang*

Key Laboratory of Automobile Materials (Jilin University), Ministry of Education, and School of Materials Science and Engineering, Jilin University, Changchun 130022, China

Transition-metal hydroxides (TMHOs) or oxides (TMOs) with layered crystalline structures are attractive electrode materials for high-density charge storage in electrochemical supercapacitors. However, their randomly stacked nanostructures on conductive reinforcements, typically carbon materials, exhibit only modest enhancement of rate capability because of poor electron and ion transports that are limited by highly anisotropic conductivity, excessive grain boundaries and weak TMHO or TMO/C interfaces. Here we report a hybrid electrode design to tackle all three of these problems in layered $Ni(OH)_2$ for high-performance asymmetric supercapacitors, wherein the single-crystalline $Ni(OH)_2$ nanosheets are vertically aligned on three-dimensional bicontinuous nanoporous gold skeleton with epitaxial Au/$Ni(OH)_2$ interfaces (NP Au/VA $Ni(OH)_2$). As a result of the unique nanoarchitecture, the pseudocapacitive behavior of $Ni(OH)_2$ is dramatically enhanced for ensuring a volumetric

capacitance as high as ~2911 F cm^{-3} (~2416 F g^{-1} for the constituent $Ni(OH)_2$) in the NP Au/VA $Ni(OH)_2$ electrode with excellent rate capability. Asymmetric supercapacitors assembled with this NP Au/VA $Ni(OH)_2$ electrode and the activated carbon have a high gravimetric energy of 31.4 Wh kg^{-1} delivered at an exceptionally high power density of 100 kW kg^{-1} with excellent cycling stability.

* Correspondence and requests for materials should be addressed to X.Y.L. (email: xylang@jlu.edu.cn) or Q.J. (email: jiangq@jlu.edu.cn).

Supercapacitors (SCs) have attracted much attention as an electrical energy storage system because they can offer higher power density than batteries, and higher energy density than conventional capacitors with long lifetime and good safety.[1-4] These fascinating features make them promising energy storage devices when high power demands are needed in hybrid vehicles, portable electronic devices and renewable energy applications.[5-7] However, the capacitive energy storage by ionic adsorption/desorption (electric double-layer capacitance, EDLC) occurring at conductive materials with large surface area, typically nanostructured carbon, suffers from a key limitation that is the low energy-density storage, in particular for the devices with a limited area or volume.[8-11] For this reason, there is considerable interest in maximizing the device capacitance (C) and extending the cell voltage (V) of SCs for an aim at increasing the energy density (E) without sacrificing the power density and cycle life according to the equation $E = CV^2/2$.[2-4,12] To increase V, a promising approach is to develop asymmetric SC (ASC) devices by employing a battery-type faradaic electrode as energy source and a capacitive electrode as a power source in aqueous electrolytes with the advantages of high ionic conductivity, non-flammability and safety.[13,14] This is a more attractive alternative to the utilization of organic electrolytes because of their intrinsic defects of flammability, low conductivity and high toxicity, in spite of a wider voltage window up to ~3 V.[2-4] Moreover, the pseudocapacitive materials, which store and deliver charge by fast and reversible redox reactions at electrode/electrolyte interface (pseudocapacitance) with specific capacitances about one order of magnitude higher than carbon-based electrodes,[15-22]

are beneficial for further enhancing the specific capacitance and energy density of ASCs. Hitherto, various ASC systems have been explored in aqueous electrolytes, wherein activated carbon (AC) and pseudocapacitive materials such as transition-metal hydroxides (TMHOs), oxides (TMOs) and conductive polymers are employed as negative and positive electrode materials, respectively.[23-28]

Owing to the poor conductivity of pseudocapacitive materials, electron transport in the positive electrode remains primarily challenging to fulfill the demand of high-energy storage at rapid charge/discharge rates in ASC devices. This problem is prominent for the layered crystalline TMHOs or TMOs because of their highly anisotropic conductivity between the inter- and intra-layer.[29-32] In contrast with the intra-layer close-packed plane favoring the electron transfer, the inter-layer electron hopping efficiency (H) of layered TMHOs or TMOs exponentially decreases as a function of the interlayer distance L, *i.e.*, $H = \exp(-2kL)$, where $k = (2m_eV_o)^{1/2}/\hbar$ with m_e the effective mass of electrons, V_o the potential barrier and $\hbar$ the Planck constant.[33-37] Although great efforts have gone into alleviating this deficiency by incorporating conductive reinforcements, such as carbon nanostructures including activated carbon, carbon nanotubes and graphene,[38-40] there still exist high contact resistance at the weak TMO or TMHO/C interfaces. Furthermore, the layered TMO or TMHO electroactive phases also suffer from poor ion accessibility and electron transfer because of undesirably excessive grain boundaries and highly anisotropic conductivity in their randomly stacked nanostructures.[38,41] These high resistances lead

to only modest enhancements in pseudocapacitive performance and rate capability in low-dimensional nanocomposite electrodes. Therefore, it is desirable to simultaneously address these resistances in the development of hybrid electrodes for high-energy storage in ASC devices at high charge/discharge rates. This requires the layered TMO or TMHO nanocrystals integrating on conductors not only with charge-transfer enhanced coherent interfaces but also along a highly conductive direction when maintaining extremely large surface areas of electrode/electrolyte. Nanostructured metals, such as Au, are the best alternative conductors because of their versatile crystalline planes, which offer various lattices matching with these of electroactive TMOs or TMHOs for producing epitaxial metal/TMO or TMHO interfaces.[42-46] While the electron and ion transports in the layered electroactive TMOs or TMHOs rely on a rational configuration,[38,41] *i.e.*, single-crystalline nanostructure grown along highly conductive direction, which can circumvent the influences of grain boundaries and conductive anisotropy. These architectural features are expected to reduce ion transport distance and facilitate the fast electron transfer from the electroactive TMOs or TMHOs to metal conductors, and thus lead to outstanding electrochemical performance of hybrid electrodes.

Here we demonstrate a design of hybrid electrodes to realize these requirements in a model system of layered crystalline TMHOs, α-$Ni(OH)_2$, for high-performance ASC applications in view of its advantages such as high theoretical specific capacitance, environmental friendliness and natural abundance. By using strong adsorption of

negatively charged surfactant on the positively charged layered facets, the single-crystalline $Ni(OH)_2$(001) nanosheets are controllably and vertically aligned on three-dimensional (3D) bicontinuous nanoporous Au skeleton (NP Au/VA $Ni(OH)_2$). Therein, the core Au network interpenetrates in the whole hybrid electrodes, not only facilitating electron and ion transports but also offering abundant coherent interfaces of Au(111)/$Ni(OH)_2$(100) with enhanced electron transfer. As a consequence, the NP Au/VA $Ni(OH)_2$ electrode exhibits a volumetric capacitance as high as ~2911 F cm^{-3} (~2416 F g^{-1} for the constituent $Ni(OH)_2$) at 6.7 A cm^{-3} and retains ~62% of initial capacitance as the current density increases to 333.3 A cm^{-3}. Asymmetric supercapacitors consisting of the NP Au/VA $Ni(OH)_2$ and AC electrodes deliver an exceptionally high power density of 100 kW kg^{-1} while maintaining a gravimetric energy of 31.4 Wh kg^{-1} with exceptional cycling stability.

Results and discussion

The NP Au/VA $Ni(OH)_2$ hybrid electrodes are fabricated by electroless plating $Ni(OH)_2$ nanosheets onto 3D bicontinuous NP Au skeleton, as schematically illustrated in **Fig. 1a**, wherein the passivating reagent of $S_2O_8^{2-}$ is introduced for the controllably vertical growth of $Ni(OH)_2$ nanosheets. Briefly, the NP Au films with pore size of ~40 nm are firstly prepared by chemically de-alloying 100-nm-thick white gold ($Au_{35}Ag_{65}$, at%) leaves in concentrated HNO_3 (Supplementary **Fig. S1**). The cost of a piece of commercial white gold leaf (20 cm × 20 cm × 100 nm) is about $0.1. They are used as 3D conductive networks because of their unique nanostructure

consisting of interconnective gold ligaments and nanopore channels, which enlist the whole network to exhibit excellent electrical conductivity up to 1.8×10^5 S cm^{-1} and offer sufficient room for the loading of electroactive materials without any polymer binder.[42,47,48] The incorporation of $Ni(OH)_2$ nanosheets into NP Au skeleton is carried out by introducing NH_3 gas through NP Au films that float on the surface of a mixed solution containing 2 mM Ni^{2+} and 0.1 mM $S_2O_8^{2-}$ ions. With the adjustment of pH value by NH_3, the layered crystalline $Ni(OH)_2$ with positive charge begins nucleating on the curved ligaments of NP Au,[49,50] and the $S_2O_8^{2-}$ ions selectively adsorb on $Ni(OH)_2(001)$ for passivating the growth of nanosheets in the [0001] direction.[51] **Figs. 2a,b** show representative top-view and cross-sectional scanning electron microscope (SEM) images of as-prepared NP Au/VA $Ni(OH)_2$, legibly revealing the uniform distribution of $Ni(OH)_2$ nanosheets with length of ~20 nm on NP Au with the maintenance of open nanoporosity. High-resolution transmission electron microscope (HRTEM) image of NP Au/VA $Ni(OH)_2$ reveals the single-crystalline nature of the constituent $Ni(OH)_2$ nanosheets (**Fig. 2c**), which is verified by the fast Fourier transform (FFT) pattern (inset of **Fig. 2c**). With the aid of passivating adsorption of $S_2O_8^{2-}$ on the (001) facet,[51] the single-crystalline $Ni(OH)_2$ nanosheets vertically align on the curved Au ligaments (**Fig. 2c**) with a layered structure consisting of close-packed oxygen planes with an ABAB stacking sequence. The Ni atoms occupy octahedral sites between alternating oxygen layers to form NiO_2 host, and the hydrogen atoms reside in the tetrahedral sites between oxygen atoms.[52] **Fig. 2d** presents HRTEM image of Au/$Ni(OH)_2$ interface, in which the interplanar spacings of

0.228 and 0.232 nm correspond to the lattice planes of $Ni(OH)_2$(100) and Au(111), respectively. The mismatch of ~2% enables the coherent combination of $Ni(OH)_2$ with Au by end-bonded contact,[53] and their proper alignments between the Fermi level in Au (the work function of ~5.2 eV) and the conduction and valence bands in the constituent $Ni(OH)_2$ (the band gap of 3.5 eV and the electron affinity of 1.47 eV) makes an Ohmic contact.[53,54] These structural and electronic properties at the Au/$Ni(OH)_2$ interface enable the hybrid electrode to not only possess stable interface structure but also exhibit excellent electron transfer capability.[53,54]The structure of vertical alignment of $Ni(OH)_2$ nanosheets on the Au ligaments of NP Au skeleton is further confirmed by X-ray diffraction (XRD) spectrum, where the evident peak at ~12° indexes to (001) plane of α-$Ni(OH)_2$ with a layer spacing of 0.76 nm in space group *P-31m* (JCPDS 22-0444) (**Fig. 2e**).[55,56] This is in distinct contrast with the XRD pattern (**Fig. S2a**) of randomly aligned $Ni(OH)_2$ nanocrystals on NP Au skeleton (NP Au/RA $Ni(OH)_2$) during the hydrolyzing process in the absence of $S_2O_8^{2-}$ (**Fig. S2b,c**). The presence of Au, Ni and O elements in the NP Au/VA $Ni(OH)_2$ electrode is demonstrated by X-ray photoelectron spectroscopy (XPS) survey (**Fig. S3**) and energy-dispersive X-ray spectrometer (EDS) analysis (**Fig. S4**). The chemical state of Ni element is verified by high-resolution XPS spectrum of Ni 2*p* region, as shown in **Fig. 2f**. There are two major peaks with binding energies at 873.1 and 855.4 eV, which correspond to Ni $2p_{1/2}$ and Ni $2p_{3/2}$ of $Ni(OH)_2$ with a separation of 17.7 eV, respectively, in addition to two satellite peaks.[57]

To evaluate the pseudocapacitive properties of the NP Au/VA $Ni(OH)_2$ films, electrochemical measurements are carried out in a three-electrode cell with a Ag/AgCl reference electrode and a Pt counter electrode in 1 M KOH aqueous electrolyte. **Fig. 3a** shows typical cyclic voltammetry (CV) curves for NP Au/VA $Ni(OH)_2$ electrodes at various scan rates up to 1000 mV s^{-1}, exhibiting much higher current density and less positive and negative shifts of redox peaks than these for the nanocrystalline $Ni(OH)_2$ randomly stacked on NP Au skeleton (NP Au/RA $Ni(OH)_2$) and carbon fiber papers (CFP/RA $Ni(OH)_2$) as well as the VA $Ni(OH)_2$ supported by CFP(CFP/VA $Ni(OH)_2$) (**Fig. 3b and Fig. S5**), which are prepared by the same method with/without the aid of $S_2O_8^{2-}$ (**Fig. 1b** and *see* experimental section for details). Furthermore, all CV curves of NP Au/VA $Ni(OH)_2$ in a wide range of scan rates consist of a pair of well-defined redox peaks corresponding to the reversible reactions of Ni(II) ↔ Ni(III), *i.e.*, $Ni(OH)_2 + OH^- \leftrightarrow NiOOH + H_2O + e^-$, implying that the capacitive characteristics are mainly governed by faradaic redox reactions. With the increasing of scan rate, the voltage shifts of redox peaks suggest a rate-controlling process for the redox reversibility of the hybrid electrode.[43,57,58] Even the scan rate increases by 200 times (from 5 to 1000 mV s^{-1}), the anodic (E_O) and cathodic (E_R) peaks only shift to 0.494 and 0.188 V, respectively, from 0.344 and 0.269 V at 5 mV s^{-1} (**Fig. 3a**). The difference between E_O and E_R ($\Delta E_p = E_O - E_R$) for NP Au/VA $Ni(OH)_2$ electrode is much lower than these for both NP Au/RA $Ni(OH)_2$ and CFP/VA $Ni(OH)_2$ electrodes at various scan rates ranging from 5 to 1000 mV s^{-1} (**Fig. S6**), implying an excellent rate capability and reversibility of VA $Ni(OH)_2$ supported by NP Au due to the

enhanced transports of electrons and ions in this hybrid electrode.[23,26,54,59] The outstanding power characteristic of the NP Au/VA $Ni(OH)_2$ hybrid electrodes results from the unique nanoarchitecture, in which the single-crystalline $Ni(OH)_2$ nanosheets vertically aligned on 3D nanoporous skeleton with coherently interfacial structure not only facilitate the fast ion accessibility but also enhance the electron transfer. However, when too much $Ni(OH)_2$ is incorporated into NP Au skeleton by increasing the concentration of the precursor $NiCl_2$ to 5 mM from 2 mM, the excess $Ni(OH)_2$ seals the nanopore channels and prevents effective contact between the nanocrystalline $Ni(OH)_2$ and the electrolyte.[42,45] This eventually leads to reductions in the current density and the rate capability (**Fig. S7**).

Fig. 3c shows galvanostatic charge/discharge curves of the NP Au/VA $Ni(OH)_2$ electrode at various current densities. In order to avoid an overestimation of the specific capacitance due to an oxygen evolution reaction (OER) at the high potential range,[60] the measurements of charge and discharge are performed in a slightly narrower voltage window (0-0.45 V). The voltage plateaus agree well with the redox peaks observed in the CV curves (**Fig. 3a**), further confirming the primary contribution of pseudocapacitive charge storage. The volumetric capacitance of the NP Au/VA $Ni(OH)_2$ electrodes can be calculated on the basis of the charge/discharge curves in **Fig. 3c** and the results are plotted in **Fig. S8**. As a consequence of the highly compact structure, the NP Au/VA $Ni(OH)_2$ electrode exhibits a volumetric capacitance as high as ~2911 F cm^{-3} at a charge/discharge current density of 6.7 A cm^{-3} with a

retention of ~62% (~1800 F cm^{-3}) even at 333.3 A cm^{-3}, much higher than those electrode materials reported previously: 376 F cm^{-3} for 3D high-density porous carbon,[61] ~500 F cm^{-3} for NP Ni/$Ni(OH)_2$,[43] and ~800 F cm^{-3} for 3D NP $Ni(OH)_2$.[19] The exceptionally high volumetric capacitance is due to the full use of high pseudocapacitance (~2416 F g^{-1} at 6.7 A g^{-1}) of the constituent $Ni(OH)_2$ in the 3D NP Au/VA $Ni(OH)_2$ hybrid electrodes. Even when the current density increases up to 333.3 A g^{-1}, the specific capacitance still retains as high as ~1644 F g^{-1} (**Fig. 3d**). They are ~1.2 times higher than that of NP Au/RA $Ni(OH)_2$ (~2076 F g^{-1} at 6.7 A g^{-1} and ~1407 F g^{-1} at 333.3 A g^{-1}) and 4 times higher than that of CFP/RA $Ni(OH)_2$ (~585 F g^{-1} at 6.6 A g^{-1} and ~251 F g^{-1} at 133 A g^{-1}) (**Fig. 3d**) due to the enhanced electrochemical kinetics, which is demonstrated by their comparison of electrochemical impedance spectroscopy (EIS) spectra (**Fig. S9**). At very high frequencies, the intercept at real part represents an intrinsic resistance, including the ionic resistance of electrolyte and the resistance of the hybrid electrode. Owing to different stack structure of crystalline $Ni(OH)_2$, the NP Au/VA $Ni(OH)_2$ electrode has a lower intrinsic resistance than NP Au/RA $Ni(OH)_2$ as well as CFP/RA $Ni(OH)_2$ (inset of **Fig. S9**). This difference will give rise to distinct ion transport capability in the electroactive $Ni(OH)_2$ phase. As shown in **Fig. S9**, the NP Au/VA $Ni(OH)_2$ electrode exhibits a more sharp increase in the imaginary part of EIS at low frequency, which implies an enhanced ion transport in VA $Ni(OH)_2$ in comparison with RA $Ni(OH)_2$. Therefore, the NP Au/VA $Ni(OH)_2$ electrode exhibits superior rate capability compared with the state-of-the-art nanostructured $Ni(OH)_2$-based hybrid electrodes,

including graphite/amorphous $Ni(OH)_2$,[23] Ni foil/3D $Ni(OH)_2$,[25] graphene/$Ni(OH)_2$,[38] $Ni(OH)_2$ nanostructures deposited with Au nanoparticles,[54] 3D graphite foam/$Ni(OH)_2$,[58] Ni foam/CoO/$Ni(OH)_2$,[62] and 3D graphene/Ni_3S_2/$Ni(OH)_2$ electrodes (**Fig. S10**).[63]

To further demonstrate the practical application of NP Au/VA $Ni(OH)_2$ electrodes, an ASC device is assembled by using NP Au/VA $Ni(OH)_2$ and AC electrodes as positive and negative electrodes, respectively. Here the AC electrode is mass-optimized to balance the charge storage with that of the positive NP Au/VA $Ni(OH)_2$ electrode by making use of EDLC in its high surface area, and its electrochemical measurements are performed in the three-electrode cell using KOH aqueous electrolyte. Owing to fast diffusion of electrolyte ions into the electrode, the AC electrode exhibits ideal capacitive behavior in a voltage range of -1~0 V with a good rate capability (**Fig. S11**). No obvious *iR* drop is observed in any of the curves, indicating that the electrode has low internal resistance. These interesting electrochemical properties ensure the outstanding performance of the ASC device based on the AC and NP Au/VA $Ni(OH)_2$ electrodes in a stable voltage window extending to as high as 1.6 V (**Fig. S12**). **Fig. 4a** presents the typical CV curves of the ASC device at various scan rates of 10-500 mV s^{-1} measured between 0 and 1.6 V in 1 M KOH aqueous electrolyte. The specific capacitance of the asymmetric cell (based on the total mass of the active materials of the two electrodes) at different scan rates is shown in **Fig. 4b**. The specific capacitance of the ASC device reaches 143 F g^{-1} at a scan rate of 10 mV s^{-1} and

retains ~81% (116 F g^{-1}) at a high scan rate of 500 mV s^{-1}, demonstrating an excellent rate capability due to the pseudocapacitive and capacitive contributions of both NP Au/VA $Ni(OH)_2$ and AC electrodes. This feature is also observed in the representative galvanostatic charge/discharge measurements of ASC device with linear and nonlinear voltage stages at different current densities (**Figs. 4c,d**). The slightly low Coulombic efficiency (CE) at low current densities is probably due to the occurrence of OER at high potential range.[60] While the current density increases to 12.5 A g^{-1}, the CE reaches ~90%, enabling this ASC device to deliver high levels of electric power. The specific energy and power of the NP Au/VA $Ni(OH)_2$//AC ASC device are plotted in the Ragone plot (**Fig. 4e**). This ASC device has a maximum energy density of 52.3 Wh kg^{-1} at low powers, and can maintain 31.4 Wh kg^{-1} at an exceptionally high power of 100.0 kW kg^{-1}, which is about sevenfold higher than those of other typical $Ni(OH)_2$-based ASC devices with the similar energy densities reported previously: graphite/amorphous $Ni(OH)_2$//AC,[23] Ni foam/CNT/$Ni(OH)_2$//AC,[24] Ni foil/3D $Ni(OH)_2$//AC,[25] graphite paper/NiCo-carbonate hydroxide nanowires/NiCoAl hydroxide nanoplates//AC electrods,[26] graphene/$Ni(OH)_2$//graphene,[57] and graphene/NiCo hydroxide//AC.[64] Taking the mass of NP Au into account, this ASC device still delivers an energy density of 14.0 Wh kg^{-1} at a high power density of 44.4 kW kg^{-1}. It is known that long cycling life is an important requirement for supercapacitors. The cycling stability of NP Au/VA $Ni(OH)_2$//AC ASC device is performed at a current density of 25.0 A g^{-1} over 10,000 cycles. **Fig. 4f** shows the capacitance retention ratio of the ASC device as a function of cycle number. After

10,000 cycles, there is only ~16% deterioration of the initial specific capacitance with the CE decreasing from 95% to ~90% (**Fig. S13**). The excellent electrochemical durability results from the stable 3D nanoporous architecture of the hybrid electrode with a solid Au/$Ni(OH)_2$ interface. As shown in **Fig. S14**, the microstructure of the hybrid electrode after long-term cycling does not show remarkable change in comparison with the initial one (**Fig. 2a**).

The exceptional performance of NP Au/VA $Ni(OH)_2$//AC ASC device can be attributed to the unique nanoarchitecture of NP Au/VA $Ni(OH)_2$ electrode with the enhanced pseudocapacitive behavior. On one hand, the single-crystalline $Ni(OH)_2$ nanosheets vertically aligned on Au ligaments with coherent interfaces facilitate the ion accessibility and electron transfer; on the other hand, the 3D bicontinuous NP Au skeleton with extremely large specific surface area of electrode/electrolyte interface and high conductivity not only offers the short ion diffusion but also accelerates transports of both ions and electrons in the whole electrodes. The unique nanoarchitecture realizes the highly efficient energy storage/deliver by minimization of internal resistances for electron and ion transports, in particular at the interfaces of conductor/active material and active material/active materials, which generally present extensively in low-dimensional nanostructures. Moreover, the stable coherent Au/$Ni(OH)_2$ interface ensures the structure stability during the long-term electrochemical cycle.

Conclusions

In summary, we have developed additive-free NP Au/VA $Ni(OH)_2$ hybrid electrodes by controllably electroless plating method for high-performance asymmetric supercapacitors. As a consequence of the unique electrode structure, in which $Ni(OH)_2$ nanosheets vertically aligned on the Au ligaments of NP Au skeleton with coherent interfaces, the NP Au/VA $Ni(OH)_2$ electrode exhibits exceptionally high volumetric capacitance of ~2911 F cm^{-3} by fully utilizing the ultrahigh pseudocapacitance of $Ni(OH)_2$ nanosheets, and excellent rate capability due to the enhanced transports of electrons and ions in the whole electrode. These properties enlist the ASC device constructed with this NP Au/VA $Ni(OH)_2$ electrode as positive electrode and AC electrode as negative electrode to show high gravimetric energy (31.4 Wh kg^{-1}) delivered at an exceptionally high power of 100 kW kg^{-1} with excellent cycling stability. The high performance makes NP Au/VA $Ni(OH)_2$ electrode as a promising electrode for thin-film energy storage devices.

Experimental section

***Fabrication of NP Au, NP Au/VA Ni(OH)$_2$, NP Au/RA Ni(OH)$_2$, CFP/VA Ni(OH)$_2$, CFP/RA Ni(OH)$_2$ and AC electrodes*.** Free-standing NP Au films with dimensions of ~ 1 cm × 1 cm were fabricated by chemically de-alloying 100-nm-thick $Au_{35}Ag_{65}$ (at%) sheets in a 70% HNO_3 solution for ~10 h at room temperature. The residual acid in NP Au film was removed by water rinsing. The NP Au/VA $Ni(OH)_2$ and Au/RA $Ni(OH)_2$ hybrid electrodes were prepared by a facile electroless plating method, in which NP Au films were floated on an aqueous solution containing 2 mM $NiCl_2$ with or without 0.1 mM $K_2S_2O_8$, and NH_3 gas evaporated from ~8 wt% aqueous ammonia was introduced to the airtight box (~0.7 L) at room temperature for 100 minutes. CFP/VA $Ni(OH)_2$ and CFP/RA $Ni(OH)_2$ electrodes were prepared by the same procedure and conditions except that a 5 mM $NiCl_2$ solutions with or without 0.25 mM $K_2S_2O_8$ were used. The mass loadings of $Ni(OH)_2$ on NP Au and CFP are 0.012 mg cm^{-2} and 0.038 mg cm^{-2}, which were determined by ICP measurement. The AC electrode was firstly prepared by mixing 80 wt% AC, 10 wt% carbon black and 10 wt% poly(vinylidene fluoride) (PVDF) binder in *N*-methyl-pyrrolidinone (NMP) solution. Then, the mixture was pasted onto a Ni foam current collector and dried at 80 °C. The mass loading for AC electrode was directly determined by comparing the mass difference before and after the mixture coating.

Structure characterization. The microstructure of the specimens were investigated using a field-emission scanning electron microscope (FESEM, JEOL 6700F)

equipped with an energy-dispersive X-ray spectrometer (EDS), and a transmission electron microscope (TEM, JEOL JEM-2100F). X-ray photoelectron spectroscopy (XPS) was determined on an ESCAlab220i-XL electron spectrometer from VG Scientific using Al Kα radiation. Weight determination was performed using a Multityple Inductively Coupled Plasma Emission Spectrometer (Shimadzu ICPE-9000). X-ray diffraction (XRD) measurement was carried out on a Rigaku D/max2500 diffractometer using Cu Kα radiation.

Electrochemical characterization. The electrochemical measurements were performed in a three-electrode configuration with a Ag/AgCl reference electrode and a Pt counter electrode. NP Au/VA $Ni(OH)_2$, NP Au/RA $Ni(OH)_2$ films are shifted on the current collectors of Au plates as working electrodes. Asymmetric supercapacitor was assembled with the NP Au/VA $Ni(OH)_2$ as a positive electrode and AC as a negative electrode. The electrolyte for all measurements was 1 M KOH. All electrochemical tests were carried out with an electrochemical analyzer (Iviumstat electrochemical analyzer, Ivium Technology). The specific capacitance of the constituent $Ni(OH)_2$ in NP Au/$Ni(OH)_2$ electrodes was calculated according to the equation, $C_{single} = (Q_{(NPG+Ni(OH)2)}-Q_{NPG})/(m\Delta V)$, where Q is the charge obtained from the discharge process, m is the mass of $Ni(OH)_2$ in single working electrode and ΔV is the discharge voltage range. The volumetric capacitances of NP Au/VA $Ni(OH)_2$ electrodes were evaluated based on their thickness of 120 nm. The energy density (E) of the ASC device was calculated in light of $E = CV^2/2$, based on total mass of active

materials in both positive and negative electrodes. The power density of ASC devices was calculated according to $P = E/t$, where t is the discharge time.

Acknowledgements

This work was supported by National Natural Science Foundation of China (No. 51201069, 51422103), Key Project of Chinese Ministry of Education (No. 313026), and the Research Fund for the Doctoral Program of Higher Education of China (No. 20120061120042).

Reference

1. J. R. Miller and P. Simon, *Science*, 2008, **321**, 651-652.
2. P. Simon and Y. Gogotsi, *Nat. Mater.*, 2008, **7**, 845-854.
3. G. P. Wang, L. Zhang and J. J. Zhang, *Chem. Soc. Rev.*, 2012, **41**, 797-828.
4. L. L. Zhang and X. S. Zhao, *Chem. Soc. Rev.*, 2009, **38**, 2520-2531.
5. A. S. Aricò, P. Bruce, B. Scrosati, J. M. Tarascon and W. Van Schalkwijk, *Nat. Mater.*, 2005, **4**, 366-377.
6. S. Chu and A. Majumdar, *Nature*, 2012, **488**, 294-303.
7. Z. G. Yang, J. L. Zhang, M. C. W. Kintner-Meyer, X. C. Lu, D. Choi, J. P. Lemmon and J. Liu, *Chem. Rev.*, 2011, **111**, 3577-3613.
8. D. Pech, M. Brunet, H. Durou, P. Huang, V. Mochalin, Y. Gogotsi, P. L. Taberna and P. Simon, *Nat. Nanotechnol.*, 2010, **5**, 651-654.
9. J. Chmiola, C. Largeot, P. L. Taberna, P. Simon and Y. Gogotsi, *Science*, 2010, **328**, 480-483.
10. M. F. EI-Kady and R. B. Kaner, *Nat. Commun.*, 2013, **4**, 1475.
11. J. A. Lee, M. K. Shin, S. H. Kim, H. U. Cho, G. M. Spinks, G. G. Wallace, M. D. Lima, X. Lepró, M. E. Kozlov and R. H. Baughman, *Nat. Commun.*, 2013, **4**, 1970.
12. R. Kötz and M. Carlen, *Electrochim. Acta*, 2000, **45**, 2483-2498.
13. Z. S. Wu, W. C. Ren, D. W. Wang, F. Li, B. L. Liu and H. M. Cheng, *ACS Nano*, 2010, **4**, 5835-5842.
14. P. C. Chen, G. Z. Shen, Y. Shi, H. T. Chen and C. W. Zhou, *ACS Nano*, 2010, **4**, 4403-4411.
15. L. B. Kong, J. W. Lang, M. Liu, Y. C. Luo and L. Kang, *J. Power Sources*, 2009, **194**, 1194-1201.
16. S. L. Chou, J. Z. Wang, S. Y. Chew, H. K. Liu and S. X. Dou, *Electrochem. Commun.*, 2008, **10**, 1724-1727.
17. L. Cao, M. Lu and H. L. Li, *J. Electrochem. Soc.*, 2005, **152**, A871-A875.
18. X. Wang, C. Y. Yan, A. Sumboja, J. Yan and P. S. Lee, *Adv. Energy Mater.*, 2014,

4, 1301240.

19. Y. Yang, G. D. Ruan, C. S. Xiang, G. Wang and J. M. Tour, *J. Am. Chem. Soc.*, 2014, **136**, 6187-6190.
20. L. Yu, G. Zhang, C. Yuan and X. W. D. Lou, *Chem. Commun.*, 2013, **49**, 137-139.
21. C. Yuan, H. B. Wu, Y. Xie and X. W. D. Lou, *Angew. Chem. Int. Ed.*, 2014, **53**, 1488-1504.
22. G. Zhang and X. W. D. Lou, *Adv. Mater.*, 2013, **25**, 976-979.
23. H. B. Li, M. H. Yu, F. X. Wang, P. Liu, Y. Liang, J. Xiao, C. X. Wang, Y. X. Tong and G. W. Yang, *Nat. Commun.*, 2013, **4**, 1894.
24. Z. Tang, C. H. Tang and H. Gong, *Adv. Funct. Mater.*, 2012, **22**, 1272-1278.
25. Y. Yang, L. Li, G. D. Ruan, H. L. Fei, C. S. Xiang, X. J. Fan and J. M. Tour, *ACS Nano*, 2014, **8**, 9622-9628.
26. J. Yang, C. Yu, X. M. Fan and J. S. Qiu, *Adv. Energy Mater.*, 2014, **4**, 1400761.
27. S. J. Peng, L. L. Li, H. B. Wu, S. Madhavi and X. W. Lou, *Adv. Energy Mater.*, 2014, **5**, 1401172.
28. C. Zhou, Y. W. Zhang, Y. Y. Li and J. P. Liu, *Nano Lett.*, 2013, **13**, 2078-2085.
29. V. Srinivasan, J. W. Weidner and R. E. White, *J. Solid State Electrochem.*, 2000, **4**, 367-382.
30. G. S. Gund, D. P. Dubal, S. B. Jambure, S. S. Shinde and C. D. Lokhande, *J. Mater. Chem. A*, 2013, **1**, 4793-4803.
31. M. Nakayama, T. Kanaya and R. Inoue, *Electrochem. Commun.*, 2007, **9**, 1154-1158.
32. W. F. Wei, X. W. Cui, W. X. Chen and D. G. Ivey, *Chem. Soc. Rev.*, 2011, **40**, 1697-1721.
33. Y. F. Yu, S. Y. Huang, Y. P. Li, S. N. Steinmann, W. T. Yang and L. Y. Cao, *Nano Lett.*, 2014, **14**, 553-558.
34. Y. Jung, J. Shen, Y. H. Liu, J. M. Woods, Y. Sun and J. J. Cha, *Nano Lett.*, 2014, **14**, 6842-6849.
35. I. Terasaki, Y. Sasago and K. Uchinokura, *Phys. Rev. B*, 1997, **56**, R12685.
36. Y. Moritomo, Y. Tomioka, A. Asamitsu, Y. Tokura and Y. Matsui, *Phys. Rev. B*,

1995, **51**, 3297.

37. J. W. Zhao, X. G. Kong, W. Y. Shi, M. F. Shao, J. B. Han, M. Wei, D. G. Evans and X. Duan, *J. Mater. Chem.*, 2011, **21**, 13926-13933.
38. H. L. Wang, H. S. Casalongue, Y. Y. Liang and H. J. Dai, *J. Am. Chem. Soc.*, 2010, **132**, 7472-7477.
39. Z. Fan, J. Yan, T. Wei, L. Zhi, G. Ning, T. Li and F. Wei, *Adv. Funct. Mater.*, 2011, **21**, 2366-2375.
40. S. W. Lee, J. Kim, S. Chen, P. T. Hammond and Y. Shao-Horn, *ACS Nano*, 2010, **4**, 3889-3896.
41. D. Luo, G. S. Li, C. C. Fu, J. Zheng, J. M. Fan, Q. Li and L. P. Li, *Adv. Energy Mater.*, 2014, **4**, 1400062.
42. X. Y. Lang, A. Hirata, T. Fujita and M. W. Chen, *Nat. Nanotechnol.*, 2011, **6**, 232-236.
43. J. L. Kang, A. Hirata, H. J. Qiu, L. Y. Chen, X. B. Ge, T. Fujita and M. W. Chen, *Adv. Mater.*, 2014, **26**, 269-272.
44. W. Shi, H. Zeng, Y. Sahoo, T. Y. Ohulchanskyy, Y. Ding, Z. L. Wang, M. Swihart and P. N. Prasad, *Nano Lett.*, 2006, **6**, 875-881.
45. X.Y. Lang, H.Y. Fu, C. Hou, G.F. Han, P. Yang, Y.B. Liu, Q. Jiang, *Nat. Commun.*, 2013, **4**, 2169.
46. J.H. Han, Y.C. Lin, L.Y. Chen, Y.C. Tsai, Y. Ito, X.W. Guo, A. Hirata, T. Fujita, M. Esashi, T. Gessner, M.W. Chen, *Adv. Sci.* 2015, **2**, 1500067.
47. X. Y. Lang, L. Zhang, T. Fujita, Y. Ding and M. W. Chen, *J. Power Sources*, 2012, **197**, 325-329.
48. F. H. Meng and Y. Ding, *Adv. Mater.*, 2011, **23**, 4098-4102.
49. Q. Wang and D. O'Hare, *Chem. Rev.*, 2012, **112**, 4124-4155.
50. J. W. Lee, T. Ahn, D. Soundararajan, J. M. Ko and J. D. Kim, *Chem. Commun.*, 2011, **47**, 6305-6307.
51. J. T. Li, W. Zhao, F. Q. Huang, A. Manivannan and N. Q. Wu, *Nanoscale*, 2011, **3**, 5103-5109.
52. P. Oliva, J. Leonardi, J. F. Laurent, C. Delmas, J. J. Braconnier, M. Figlarz, F.

Fievet and A. De Guibert, *J. Power Sources*, 1982, **8**, 229-255.

53. F. Léonard, A.A. Talin, *Nat. Nanotechnol.*, 2011, **6**, 773-783.
54. S.I. Kim, P. Thiyagarajan, J.H. Jang, *Nanoscale*, 2014, **6**, 11646-11652.
55. G. G. Zhang, W. F. Li, K. Y. Xie, F. Yu and H. T. Huang, *Adv. Funct. Mater.*, 2013, **23**, 3675-3681.
56. C. H. Tang, X. S. Yin and H. Gong, *ACS Appl. Mater. Interfaces*, 2013, **5**, 10574-10582.
57. J. Yan, Z. J. Fan, W. Sun, G. Q. Ning, T. Wei, Q. Zhang, R. F. Zhang, L. J. Zhi and F. Wei, *Adv. Funct. Mater.*, 2012, **22**, 2632-2641.
58. J. Y. Ji, L. L. Zhang, H. X. Ji, Y. Li, X. Zhao, X. Bai, X. B. Fan, F. B. Zhang and R. S. Ruoff, *ACS Nano*, 2013, **7**, 6237-6243.
59. C. Z. Yuan, J. Y. Li, L. R. Hou, X. G. Zhang, L. F. Shen and X. W. Lou, *Adv. Funct. Mater.*, 2012, **22**, 4592-4597.
60. B. S. Yeo and A. T. Bell, *J. Phys. Chem. C* 2012, **116**, 8394-8400.
61. Y. Tao, X. Y. Xie, W. Lv, D. M. Tang, D. B. Kong, Z. H. Huang, H. Nishihara, T. Ishii, B. H. Li and D. Golberg, *Sci. Rep.*, 2013, **3**, 2975.
62. C. Guan, X. L. Li, Z. L. Wang, X. H. Cao, C. Soci, H. Zhang and H. J. Fan, *Adv. Mater.*, 2012, **24**, 4186-4190.
63. W. J. Zhou, X. H. Cao, Z. Y. Zeng, W. H. Shi, Y. Y. Zhu, Q. Y. Yan, H. Liu, J. Y. Wang and H. Zhang, *Energy Environ. Sci.*, 2013, **6**, 2216-2221.
64. Y. W. Cheng, H. B. Zhang, C. V. Varanasi and J. Liu, *Energy Environ. Sci.*, 2013, **6**, 3314-3321.

Figure captions

Figure 1. Schematic for the fabrication of hybrid electrodes. **(a)** NP Au/VA $Ni(OH)_2$ electrode is prepared by a modified plating method, in which single-crystalline $Ni(OH)_2$ nanosheets are vertically aligned on the curved Au ligament of NP Au skeleton with the assistance of $K_2S_2O_8$ reagent. **(b)** CFP/RA $Ni(OH)_2$ electrode is prepared by loading $Ni(OH)_2$ nanocrystals with random stack on CFP in the aqueous solution in the absence of $K_2S_2O_8$.

Figure 2. **(a)** Top-view and **(b)** cross-section SEM images of NP Au/VA $Ni(OH)_2$ electrode. **(c)** HRTEM image of the NP Au/VA $Ni(OH)_2$ electrode. Inset: The FFT pattern of the constituent $Ni(OH)_2$. **(d)** HRTEM image of Au/$Ni(OH)_2$ interfacial structure with their corresponding atomic structures. **(e)** XRD pattern and **(f)** XPS spectrum of NP Au/VA $Ni(OH)_2$ electrode.

Figure 3. **(a)** Typical CV curves of NP Au/VA $Ni(OH)_2$ electrode at various scan rates within a voltage window of 0-0.55 V. **(b)** Comparison of CV curves among NP Au/VA $Ni(OH)_2$, NP Au/RA $Ni(OH)_2$ and CFP/VA $Ni(OH)_2$ electrodes at 500 mV s^{-1}. **(c)** Galvanostatic charge-discharge profiles of NP Au/VA $Ni(OH)_2$ electrode at various current densities in a voltage window of 0-0.45 V. **(d)** Specific capacitance of constituent VA $Ni(OH)_2$ and RA $Ni(OH)_2$ on NP Au and RA $Ni(OH)_2$ on CFP substrates at various gravimetric current densities.

Figure 4. **(a)** CV curves and **(b)** average specific capacitance of NP Au/VA $Ni(OH)_2$//AC ASC device at different scan rates in a voltage window of 0-1.6 V. **(c)** Galvanostatic charge/discharge curves and **(d)** specific capacitance of NP Au/VA $Ni(OH)_2$//AC ASC device at various gravimetric current densities. **(e)** Ragone plot comparing the energy and power densities of NP Au/VA $Ni(OH)_2$//AC ASC device with those of previously reported $Ni(OH)_2$-based ASCs, such as graphite/amorphous $Ni(OH)_2$//AC,[23] Ni foam/CNT/$Ni(OH)_2$//AC,[24] Ni foil/3D $Ni(OH)_2$//AC,[25] graphite/NiCo-carbonate hydroxide nanowires/NiCoAl hydroxide nanoplates//AC electrodes,[26] graphene/$Ni(OH)_2$//porous graphene,[57] and graphene/NiCo hydroxide//AC.[64] **(f)** Cycling stability of NP Au/VA $Ni(OH)_2$//AC ASC device as a function of cycle number at a gravimetric current density of 25.0 A g^{-1}.

Figure 1.

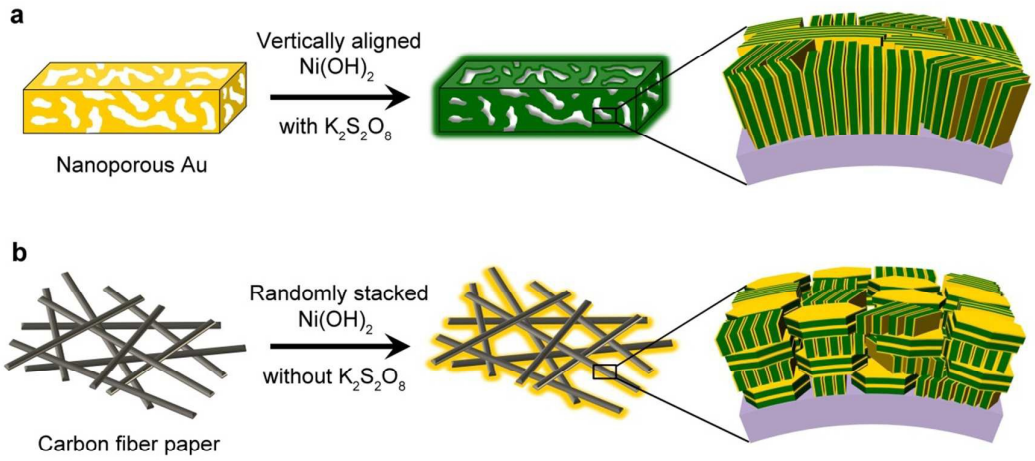

Figure 2.

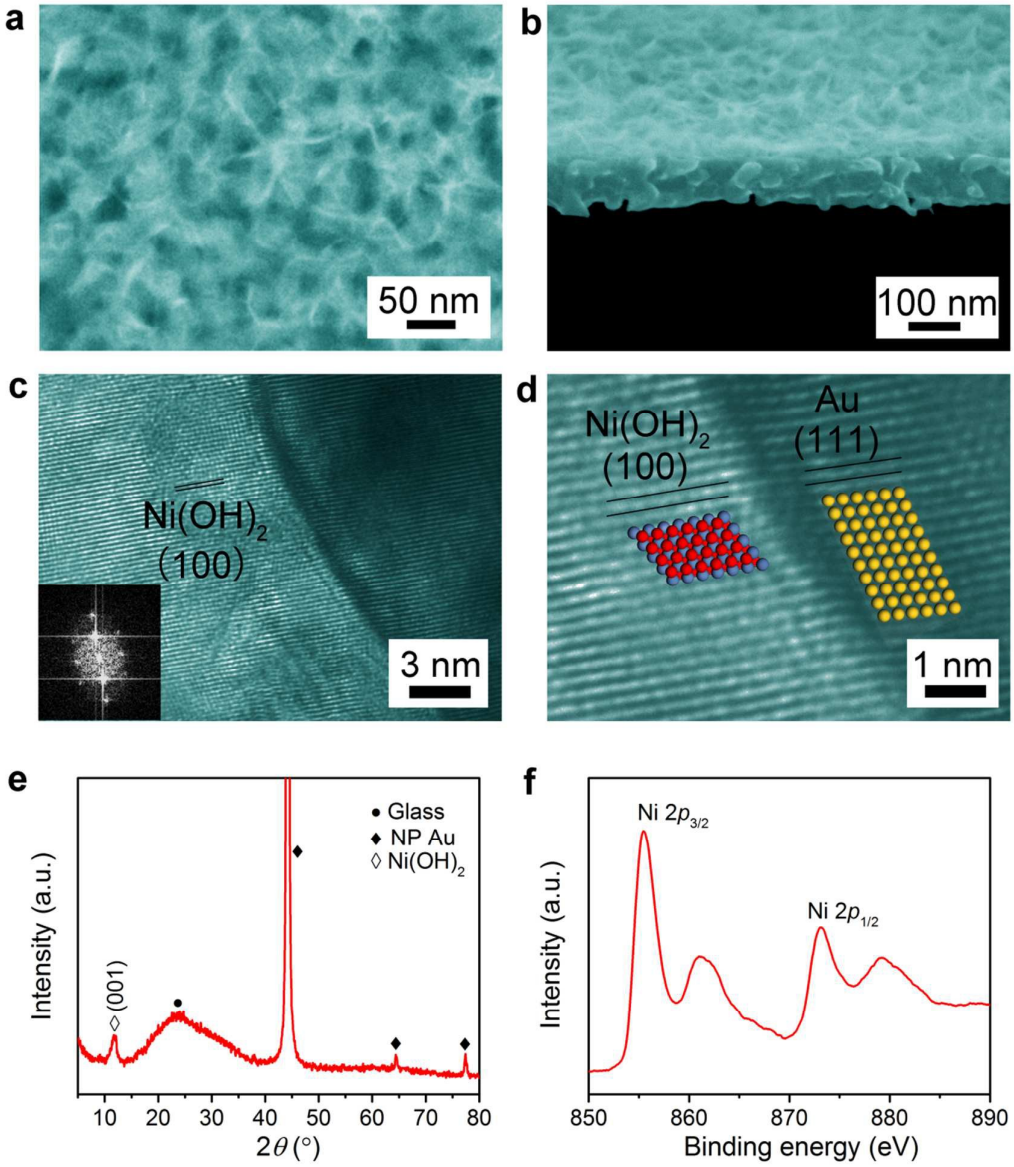

Figure 3.

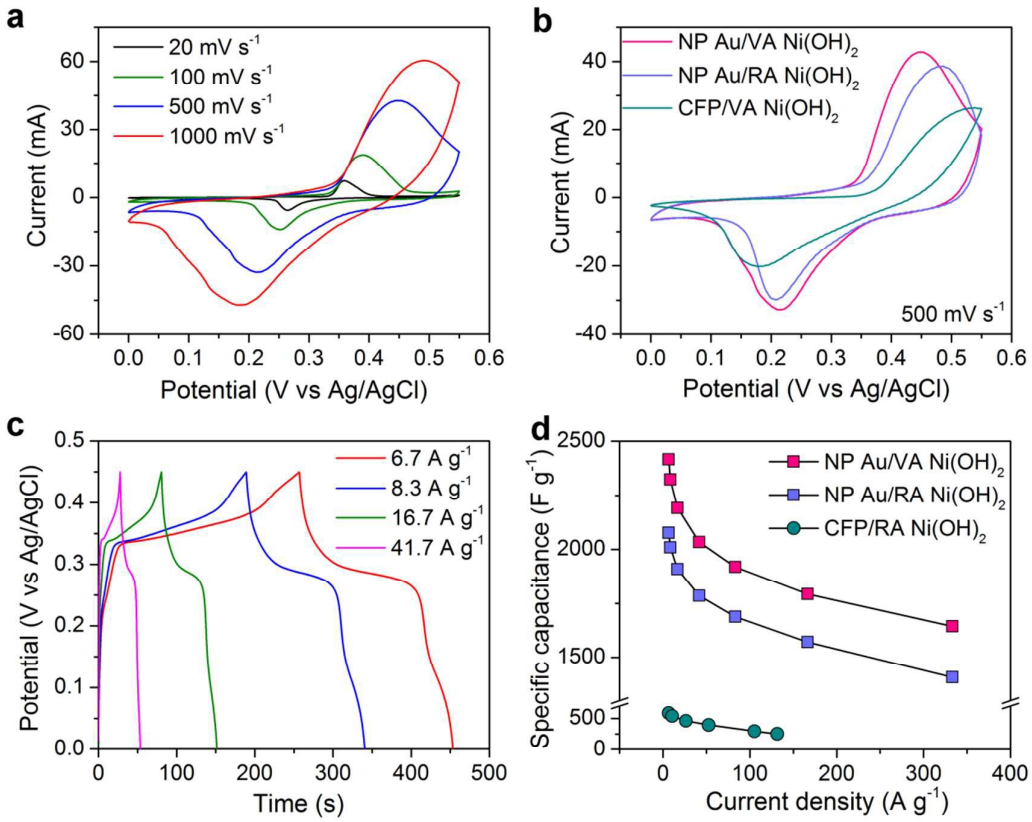

Figure 4.

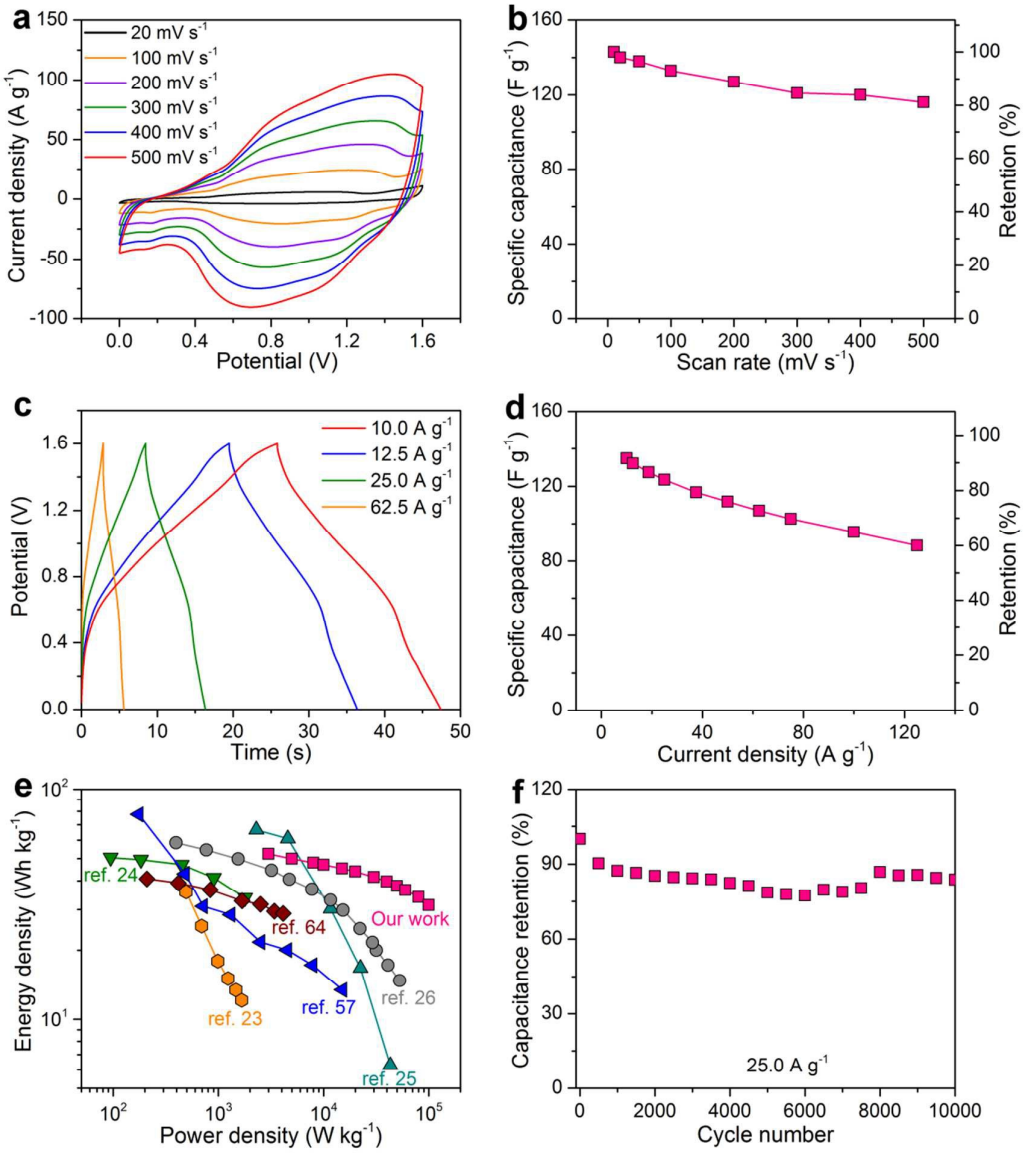

TOC

We report a rational design of hybrid electrodes with minimization of internal resistance for high-performance asymmetric supercapacitors.